

A Machine-Learning Method for Deriving State-Dependent Fragility Curves of Existing Steel Moment Frames with Masonry Infills

Jing-Ren Wu^{1*} and Luigi Di Sarno¹

¹Dept. of Civil Eng. & Industrial Design, University of Liverpool, L69 3GH, Liverpool, U.K.

*Corresponding Author. Tel.: +44 7598460022. Email address: jingren.wu@liverpool.ac.uk

Abstract

Seismic assessment of existing buildings is usually a building-specific task that relies on refined finite element models. Such a task may require considerable computational demand, especially when predicting the seismic fragility of existing buildings under the framework of performance-based earthquake engineering. However, the computational cost can be significantly reduced by replacing the finite element model with a well-trained machine learning-based model, for example, artificial neural network. This paper presents the application of feedforward neural networks to predict the maximum inter-storey drift of existing steel frames, taking into account the effects of masonry infills. It is found that the use of four-to-five commonly adopted seismic intensity measures as input parameters can be sufficient in estimating the inter-storey drift demand at each floor of a multi-storey building.

Key words: Neural Networks, Existing Steel Frames, Masonry Infills

1 Introduction

The evaluation of seismic vulnerability of structures constitutes an essential part of seismic assessment of existing steel buildings. It is usually achieved by means of fragility analysis under the framework of performance-based earthquake engineering [1]. State-dependent fragility curves are a common way to illustrate the seismic vulnerability of structures in a probabilistic manner, which describe the probability of exceeding a specific limit state given the intensity of ground motions (GMS_{DSL1}). Conventionally, the derivation of fragility curves, through either the incremental dynamic analysis (IDA) [2] or the multiple stripe analysis (MSA) [3], relies on performing a large number of nonlinear dynamic analyses to obtain the structural response, thus is computationally expensive and time-consuming. However, the rapid development of machine learning techniques has provided strong tools to reduce significantly the computation cost and time required to perform fragility analysis.

Machine learning (ML) refers to methodologies that can detect the hidden patterns behind data without being explicitly programmed in order to establish forecasting models and support decision making under uncertain conditions [4, 5]. Currently the majority of ML algorithms can be categorised into two main groups, namely supervised learning and unsupervised learning. Supervised learning uses labelled training data to develop a predictive model that is able to map a set of input data to the output data, which is usually adopted to solve classification and regression problems. On the other hand, unsupervised learning uses data without clear target labels to infer the underlying structure behind a set of data, thus is usually selected for clustering and dimensionality reduction problems [6]. In the field of earthquake engineering, the application of ML techniques has been widely demonstrated in literature to address problems such as seismic hazard analysis, system identification, fragility assessment and structural control, which have been summarised in some comprehensive reviews in the past few years [e.g., 4, 6, 7 among others].

In particular, many previous studies in literature have implemented ML models in the derivation of fragility curves for steel and reinforced-concrete moment frames to help reduce the computational cost. One of the fundamental applications of ML models in this regard is to predict the structural response based on representative intensity measures (IMs) of GMs and structural properties [8-11]. In this way, the output of ML models is usually the engineering demand parameter (EDP) required to derive the fragility curves instead of the complete time-history of structural response. Alternatively, there are also attempts to use ML models to estimate the parameters governing the fragility functions. [e.g., 12-14], such as the median and dispersion of the collapse intensity, which eventually lead to the fragility curves in a more straightforward manner. In addition, there are also a few studies using classification models to estimate the damage state of structures, *i.e.* the whether a limit state has been exceeded, thus state-dependant fragility curves can be derived in a different approach [15, 16]. Nonetheless, the majority of previous studies mentioned above did not consider the effects of infill walls on the response of framed structures, particularly in the case of assessing the vulnerability of existing steel moment frames. However, it has been reported in many previous studies [e.g., 17-19] that the presence of infill walls significantly affects the overall structural behaviour of steel frames, especially existing buildings. As the infill walls represent an essential source of the inelastic behaviour of existing steel moment frames, it can cause increased difficulty in obtaining a reliable ML model. Therefore, it is worth exploring the possibility of implementing ML models to predict the behaviour of infilled structures. On the other hand, most of the previous research has focused on the use of regression models to predict the structural response, while only a few attempts have been made to the use of classification models. Considering that the main task in the derivation of fragility curves is for each GM to determine whether the structure is safe under the limit state being assessed, which is naturally a binary classification problem. Therefore, it can be beneficial to employ

classification models in the derivation of fragility curves of existing steel moment frame, especially when the effects of infill are taken into account.

To this end, the aim of this paper is to present the use of neural network classification models to derive fragility curves of existing steel moment frames, taking into account the effects of masonry infills. Four case study buildings representing low- and mid-rise existing steel moment frames designed for low and high seismicity were selected to demonstrate the implementation of the proposed method. Fragility curves were then obtained for all the case study buildings using the proposed method and compared with the results obtained from conventional IDA in order to assess the accuracy and efficiency of the proposed method.

2 Neural Network Classification Models

Artificial neural networks (ANNs) are computing systems developed to imitate the way human brains process information and perform tasks including pattern recognition, data classification and forecast of future events. An ANN typically contains three types of layers, namely the input layer, hidden layer and output layer. Each layer consists of nodes similar to biological neurons, where the input data are processed through the application of weights, biases and activation functions in order to create a nonlinear model.

A feedforward neural network (FNN) is a typical type of ANNs that contains one input layer, one or a few hidden layers and one output layer. In the present study, a fully connected FNN classification model with one hidden layer is adopted, whose structure is schematically demonstrated in [Figure 1](#). It can be seen that each node in the hidden layer receives inputs from all the nodes in the input layer and subsequently produces a single output that is sent to each node in the output layer. Also, as suggested by its name, FNN models only allow data to move forward from the input layer to the output layer through the hidden layer. A detailed description of the fully connected FNN is provided herein.

Input Layer:

The input layer is where the predictor data are provided to the FNN model, and the number of nodes in the input layer is equal to the number of predictor variables, which is denoted as N . As shown in [Figure 1](#), each input vector $\mathbf{X}_i = [x_1 \ x_2 \ \dots \ x_N]$ is also referred to as an observation, where each element x_i represents a predictor variable. In order to accelerate the learning process and achieve faster convergence, the predictor data are standardised with respect to the mean and standard deviation of the data before being sent to the hidden layers for further processing.

Hidden Layer:

A shallow FNN usually contains one or a few hidden layers. In the present study, as shown in [Figure 1](#), the network with a single hidden layer is considered. The data are processed in the hidden nodes based on [Eq.\(1\)](#), where $w_{i,j}$ and b_i are respectively the weights and bias applied to the j th predictor variable in the i th hidden node, and $f(x)$ represents the activation function. It is worth mentioning that the number of nodes adopted in the hidden layer is not unique and usually varies depending on the number of input and output variables. Moreover, some frequently used activation functions are also shown in [Figure 1](#), including the rectified linear unit (ReLU) function, the hyperbolic tangent (tanh) function and the sigmoid function_[DSL2]_[WJ3] (see [Figure 1](#) for definition). The use of activation functions is aimed at introducing nonlinearity into the network models to enhance their capabilities of solving nonlinear problems [10]. Therefore, the choice of activation function controls how well the network model can learn from the input data, hence influences the performance of network models.

$$n_i = f \left(\sum_{j=1}^N w_{i,j} x_j + b_i \right) \quad [1]$$

Output Layer:

The output layer is where the network model produces the prediction, which contains the same number of nodes as the output variables. It should be mentioned that the output layer processes data in a similar manner to the hidden layer, as expressed in Eq.(2), where P is the number of hidden nodes and n_i represents the output of the i th hidden node. Furthermore, in classification models, the softmax function is typically adopted as the activation function, which makes predictions based on the posterior probability of each output, *i.e.* the output corresponding to the largest posterior probability is adopted as the predicted class. The softmax function is illustrated in Eq.(3), where K is the number of class considered in the classification problem and the sum of posterior probabilities p_i from each output node should always be equal to 1.

$$p_i = f\left(\sum_{j=1}^P w_{i,j}n_j + b_i\right) \quad [2]$$

$$p_i = f(z_i) = \frac{e^{z_i}}{\sum_{j=1}^K e^{z_j}} \quad [3]$$

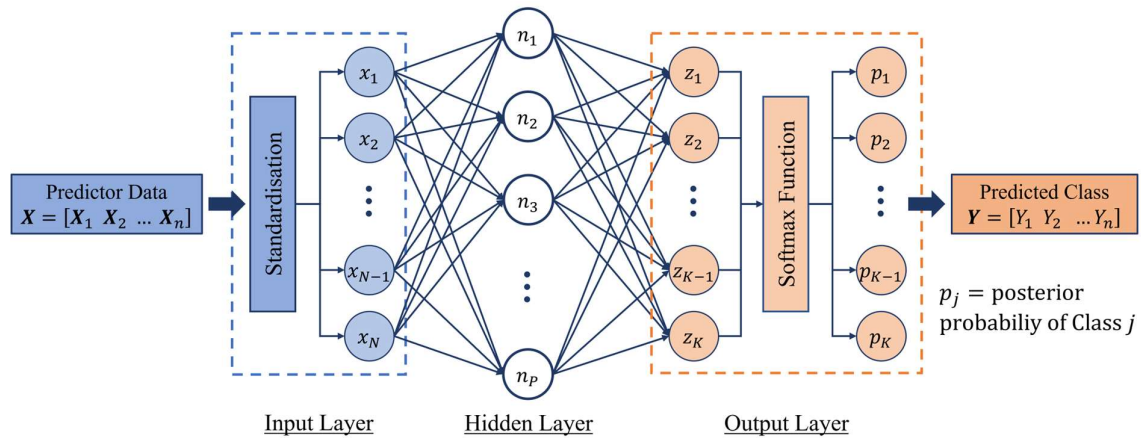
Training algorithm and Performance Evaluation Parameter:

The training of FNN models involves two essential aspects, namely the training algorithm and the performance evaluation parameter. In the present study, the limited-memory Broyden-Fletcher-Goldfarb-Shanno quasi-Newton algorithm (LBFGS) [20] is adopted as the training algorithm, which uses the Hessian matrix approach instead of the Jacobian matrix approach used by Newton method to reduce the time required to perform the optimisation task. Besides, the LBFGS algorithm only uses a limited amount of computer memory, as it utilises a matrix with reduced size compared to the one used by the original BFGS method to approximate the inverse Hessian matrix

The LBFGS algorithm optimises the FNN models based on the cross-entropy loss, which indicates the predictive inaccuracy of the FNN classification models, as defined by Eq.(4), where n is the total number of observations and y_j is an indicator, which is equal to 1 for the posterior possibility p_j corresponding to the true observed class and otherwise equal to zero.

$$Loss = -\frac{1}{n} \sum_{i=1}^n \left(\frac{1}{K} \log \left(\sum_{j=1}^K y_j p_j \right) \right) \quad [4]$$

The training of FNN models is usually based on two sets of data, which are the training data and the validation data. As suggested by the names, the FNN models learn from the training data, based on which the model properties are defined, including the weights and biases. On the other hand, the use of validation data is to accelerate the training process and to prevent over-fitting, particularly when a limited size of training data is adopted.



Common activation functions at hidden layer:

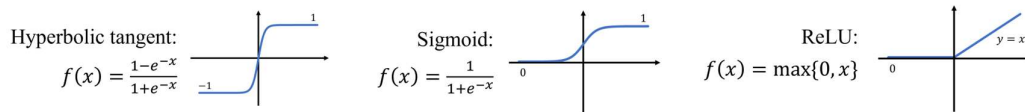


Figure 1. The structure of a feedforward neural network model with single hidden layer.

3 Proposed Framework for Deriving Fragility Curves

The proposed framework for deriving fragility curves is introduced in this section. The framework contains three main steps, as demonstrated in Figure 2, which includes numerical

modelling and pre-assessment of the infilled steel frames, training of the FNN models and lastly, the derivation of fragility curves. Details of the framework are described hereafter.

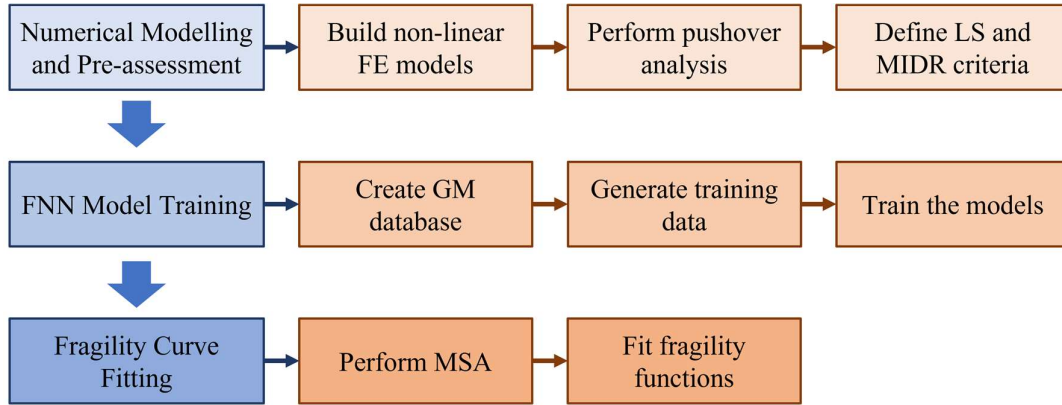


Figure 2. The proposed framework for deriving fragility curves of existing steel frames with masonry [infills][DSL4][WJ][5].

3.1 Numerical Modelling and Pre-assessment

The first step of the proposed framework is to build the finite element (FE) model and conduct preliminary assessment of the steel frame to be investigated, as demonstrated in **Figure 3**. This step is aimed to define appropriate limit states and the corresponding inter-storey drift ratio (IDR) criteria for the derivation of state-dependent fragility curves. This step further involves three sub-steps. The first is to build the FE models suitable for the nonlinear static (pushover) and dynamic (time-history) analysis. Then the monotonic behaviour of the subject structure at the storey level can be acquired by performing pushover analysis. A typical storey shear-IDR curve of infilled existing steel frames is shown in **Figure 3**, where a clear drop of shear force can be seen after the peak strength point due to failure of masonry infills. Finally, based on the results of pushover analysis, building-specific limit states can be defined by assessing the damage state of the structure at increasing lateral displacement. Alternatively, codified limit states and IDR criteria may also be adopted depending on the scope of research.

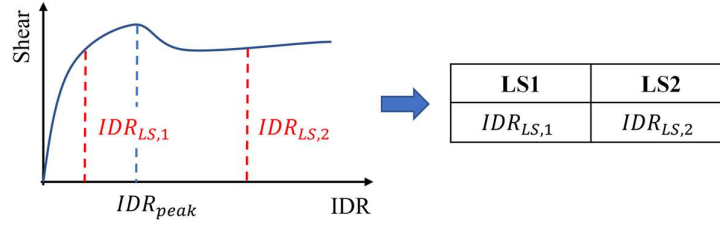


Figure 3. Definition of limit states and IDR criteria based on the pushover curve.

3.2 Training of FNN Models

The second step is to prepare the training data and establish the FNN models. A schematic diagram showing the structure of the FNN models adopted in this study is provided in [Figure 4](#), where it can be seen that the input parameters contains seven intensive measures (IMs) of GMs based on the suggestions from previous studies [10, 26]. The selected IMs were listed in [Table 1](#), including peak ground acceleration (PGA), peak ground velocity (PGV) and cumulative absolute velocity (CAV), which are determined directly from the time history of the ground motion records, and spectral acceleration at T_1 ($S_a(T_1)$), spectral displacement at T_1 ($S_d(T_1)$), velocity spectrum intensity (VSI) and effective peak ground acceleration (EPA), which can be determined from the response spectra of the records. To prepare the training data, a suite of GM records should initially be selected. In the present study, the GM records adopted by FEMA P695 [27] are used as standard GM record database, which comprises 28 near-fault GMs and 22 far-field GMs and can be acquired from the PEER database [28].

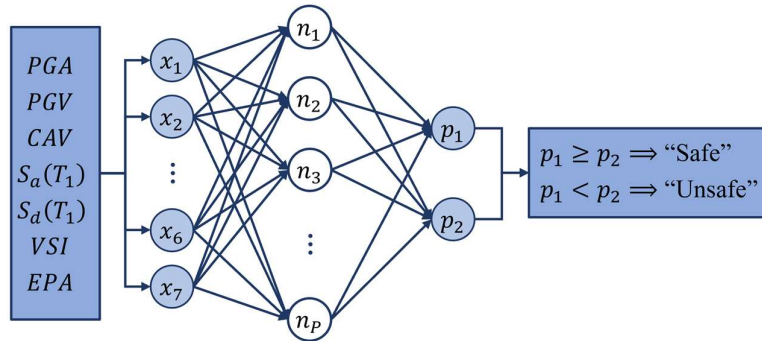


Figure 4. The structure of a feedforward neural network model with single hidden layer.

Table 1. Intensity measures of the GMs involved in the development of FNN models as input parameters.

Notation	Intensity measure	Formula
PGA	Peak ground acceleration	$\max(\ddot{x}_g)$
PGV	Peak ground velocity	$\max(\dot{x}_g)$
CAV	Cumulative absolute velocity	$\int_0^t \ddot{x}_g dt$
$S_a(T_1)$	Spectral acceleration at T_1	$S_a(T_1)$
$S_d(T_1)$	Spectral displacement at T_1	$S_d(T_1)$
VSI	Velocity spectrum intensity	$\int_{0.1}^{2.5} S_v dT$
EPA	Effective peak ground acceleration	$\frac{S_a(0.1, \dots, 0.5)}{2.5}$

Subsequently, three sets of balanced data are to be generated within this step to serve as the training data. The procedure is summarised in [Figure 5](#), where the first step is to determine the maximum IDRs (MIDRs) of the steel frame under the unscaled GM records via non-linear time-history analysis (NTHA) and also to find the median value of the MIDRs (denoted as $MIDR_{med,1}$). Then, the next step is to compute the first scaling factor (SF_1) for GM records using [Eq.\(5\)](#) and determine the corresponding MIDRs of the steel frame under the scaled GM records, whose median value is denoted as $MIDR_{med,2}$. Successively, the final set of MIDR data can be generated considering the second scaling factor (SF_2) for GM records defined in [Eq.\(6\)](#), where the coefficients a and b define the exponential function passing through the nodes ($MIDR_{med,1}, 1$) and ($MIDR_{med,2}, SF_1$). Eventually, by combining the three sets of MIDR data and labelling them as ‘Safe’ or ‘Unsafe’ based on the target limit state, the output of the training data can be obtained, while the input data are the corresponding IMs summarised in [Table 1](#).

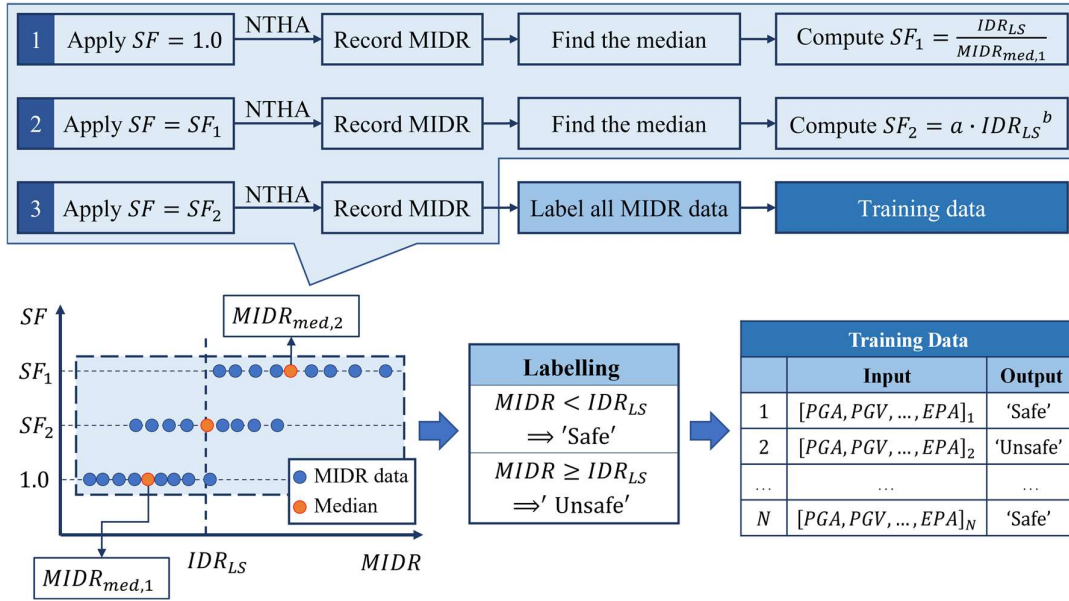


Figure 5. The procedure of generating the training and validation datasets.

$$SF_1 = \frac{IDR_{LS}}{MIDR_{med,1}} \quad [5]$$

$$SF_2 = a \cdot MIDR_{med,1}^b \quad [6]$$

Lastly, with the generated training data, the properties of FNN models can be determined through the training process introduced in the previous section. However, it should be noted that the trained FNN models are not unique due to the stochastic training algorithm, and consequently the resultant fragility curves may be slightly different from each other. Therefore, the proposed method will yield a range of potential fragility curves, whose envelopes forms a region that represents the final solution.

3.3 Derivation of Fragility Curves

The last step of the proposed framework is to derive the fragility curves by performing MSA [3]. Instead of performing further NTHA, the trained FNN models are used to directly predict whether the structure is safe or not subjected to each input IM combination. In addition, to avoid complicating the problem, the IM combinations from the selected GM records are adopted in the MSA, in which case the correlations among adopted IMs need not be clarified

as in the case of Monte Carlo simulation. The fitting of fragility curves can be achieved based on least squares or maximum likelihood, where in both cases, the incremental scaling of IMs should be stopped when failure probability reaches 90% in order to avoid over-fitting, particularly in the case of maximum likelihood method.

4 The Case Study Buildings

To demonstrate the proposed method for deriving fragility curves, four pre-Northridge buildings from the SAC Steel Project [21] were adopted as the case study buildings. The steel buildings selected for this study are the 3- and 9-storey buildings, which were designed following the local seismic codes in Boston and Los Angeles, respectively. Therefore, the Boston buildings are representatives of the steel buildings designed for low-seismicity, whilst the Los Angeles buildings represent buildings designed for high-seismicity. It is worth mentioning that the four buildings were selected for the present study because they have been widely accepted as case study buildings in previous research [e.g., 21, 22], hence were considered appropriate representatives of existing steel buildings in the United States. For convenience, the four buildings are hereafter referred to as BOS3, BOS9, LA3 and LA9, respectively for the 3- and 9-storey Boston and Los Angeles buildings.

Due to the regularities of the steel buildings in the plan layouts and along the heights, only their perimeter frames in the N-S direction were considered in this study, which are shown in [Figure 6](#), as the internal gravity frames were not considered to contribute significantly to the lateral resistance of the buildings. Besides, the profiles of beams and columns are provided in [Table 2 to 5](#). The nominal yield strength of columns is 344.5 MPa for all four buildings, whilst the nominal yield strength of beams is 248.0 MPa for Los Angeles buildings and 344.5 MPa for Boston buildings. Fully welded pre-Northridge beam-column connections are used in the moment frames, but it should be noted that the BOS9, LA3 and LA9 buildings all comprise a bay with pinned beam-column connections. The BOS3 and LA3 buildings are

fixed at the base, while the BOS9 and LA9 buildings have pinned column base connections. Moreover, as can be seen in Figure 6, both of the two 9-storey buildings have a basement floor, hence lateral constraints are also considered at the ground level of the two buildings in addition to the constraints at column bases.

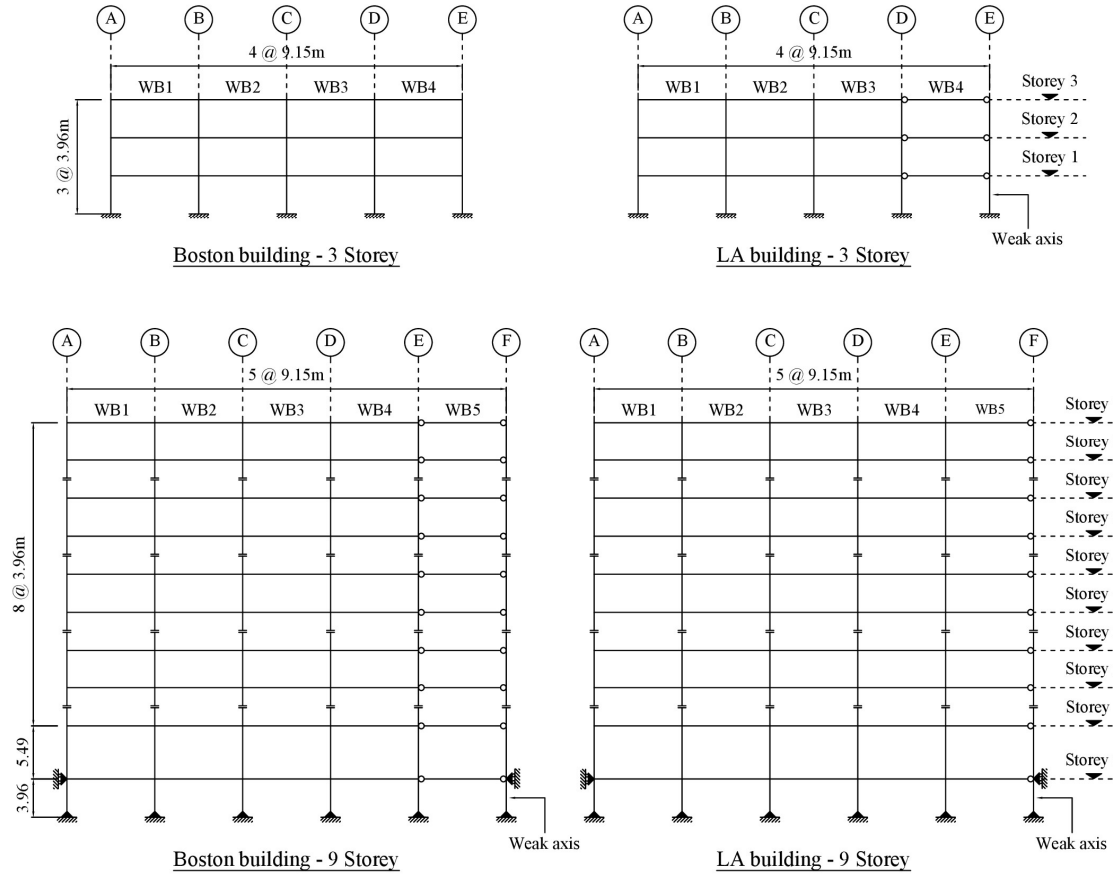


Figure 6. Geometry properties of the case study steel buildings and element profiles.

Table 2. Beam and column profiles for the BOS3 building.

Floor	Column		Beam
	A, E	B, C, D	WB1
1	W14×74	W14×99	W21×62
2	W14×74	W14×99	W21×57
3	W14×74	W14×99	W18×35

Table 3. Beam and column profiles for the BOS9 building.

Floor	Column			Beam	
	A	B, C, D, E	F	WB1	WB2
0	W14×211	W14×283	W14×211	W24×68	W24×68
1	W14×211	W14×283	W14×211	W36×135	W27×94
2	W14×159	W14×233	W14×159	W33×118	W27×84
3	W14×159	W14×233	W14×159	W30×116	W27×84
4	W14×132	W14×211	W14×132	W30×116	W24×76
5	W14×132	W14×211	W14×132	W30×108	W24×76
6	W14×99	W14×176	W14×99	W30×99	W24×68
7	W14×99	W14×176	W14×99	W27×94	W24×62
8	W14×61	W14×120	W14×68	W24×76	W24×55
9	W14×61	W14×120	W14×68	W18×40	W18×40

Table 4. Beam and column profiles for the LA3 building.

Floor	Column			Beam	
	A, D	B, C	E	WB1	WB2
1	W14×257	W14×311	W14×68	W33×118	W21×44
2	W14×257	W14×311	W14×68	W30×116	W21×44
3	W14×257	W14×311	W14×68	W24×68	W21×44

Table 5. Beam and column profiles for the LA9 building.

Floor	Column		Beam
	A, F	B, C, D, E	WB1
0	W14×370	W14×500	W36×160
1	W14×370	W14×500	W36×160
2	W14×370	W14×455	W36×160
3	W14×370	W14×455	W36×135
4	W14×283	W14×370	W36×135
5	W14×283	W14×370	W36×135
6	W14×257	W14×283	W36×135
7	W14×257	W14×283	W30×99
8	W14×233	W14×257	W27×84
9	W14×233	W14×257	W24×68

5 Implementation of the Proposed Method

5.1 FE Modelling of the Steel Buildings

2D-FE models of the case study buildings were implemented in OpenSees [23]. The FE model of the LA3 building is shown in Figure 7 as an example of the modelling scheme, where it can be seen that the FE model consisted of 2 parts, the ‘Steel Frame’ and the ‘Leaning Column’. All beams and columns of the steel frame were modelled using force-based beam-column elements with fibre sections, whose properties were defined by the *Steel01* material from the OpenSees material library. Besides, instead of using the nominal yield strength of the steel, *i.e.* 248.0 and 344.5 MPa, the corresponding expected values of the yield strength were adopted, *i.e.* 339.0 and 396.9 MPa, as suggested by Gupta and Krawinkler [21], as well as a hardening ratio of 0.02. Furthermore, the fully welded beam-column connections were assumed to be rigid in the FE models, while the pinned beam-column connections were modelled using a rotational spring with negligible stiffness. Lastly, the aforementioned boundary conditions were implemented in the FE models, including the lateral restraints applied at the ground level of the BOS9 and LA9 buildings.

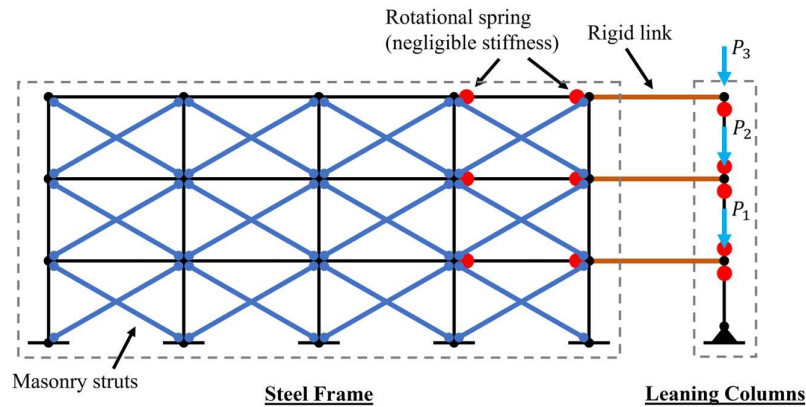


Figure 7. Illustration of the FE modelling in OpenSees: the LA3 building.

An essential part of the FE models is the modelling of masonry infills. In the present study, the masonry infills were modelled using the Liberatore-Decanini approach [24], which is illustrated in Figure 8a. The model contained a single compression-only strut in each diagonal

direction to simulate the infill wall panels, and the mechanical properties of the strut was described by a four-branch multilinear curve. Since no information of masonry infills was provided in the original document of the four steel buildings, the material properties utilised to define the single-strut model were assumed according to a previous experimental test on infilled existing steel frame [19]. The Young's modulus E_m was 7669 MPa, the vertical compression strength f_m was 2.81 MPa and the tensile strength obtained from diagonal compression tests f_t was 0.65 MPa. The properties of the masonry struts were defined using the *Hysteretic* material in OpenSees, with assumptions also made in relation to the pinching of the masonry infills. Figure 8b shows an example of the cyclic behaviour of the masonry struts. The thickness of infill walls in the BOS3 and LA3 buildings, as well as on the top five storeys of the BOS9 and LA9 buildings, was assumed to be 155 mm. For the bottom five storeys of the BOS9 and LA9 buildings, the thickness of infills was assumed to be 233 mm.

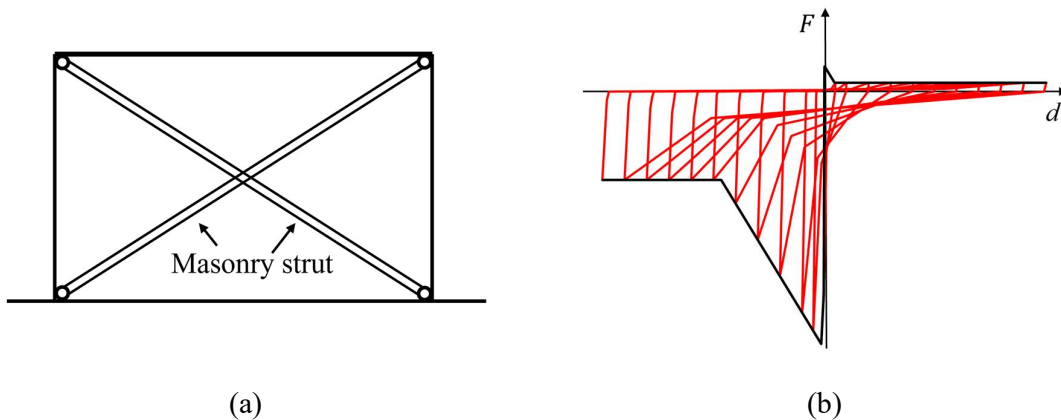


Figure 8. Demonstration of the Libertore-Decanini `model`_[DSL6] for masonry infills.

In addition to the steel frame structures, leaning columns were also introduced to the FE models to account for the P-Delta effect, as demonstrated in Figure 7. The leaning columns were modelled by rigid beam elements and were connected to the main structure through rigid truss elements (rigid links in Figure 7). Since the leaning columns were included only to account for the P-Delta effect, they were assumed to be not capable of transferring bending moment. Thus, rotational springs with negligible stiffness were also added to the ends of

leaning column to release the moment at joints. A pinned end was assumed at the base of leaning columns in all FE models.

The storey masses were assigned to each node in the main structures based on their tributary areas, *i.e.* the corner nodes were assigned half the mass of the intermediate nodes. No mass was added to the nodes in the leaning columns. On the other hand, gravity loads were applied to both the steel frame and the leaning column in each FE model. The gravity loads, which in reality were sustained by the internal gravity frames, were applied to the corresponding nodes in the leaning column, as shown in [Figure 7](#). In the meantime, the gravity loads added to the steel frame in each FE model were solely the gravity loads sustained by the frame structure, which were less significant compared to the gravity loads on the leaning column, hence are not shown in [Figure 7](#) for clarity.

5.2 Assessment of the Seismic Behaviour of the Steel Buildings

Pushover analysis was performed at the beginning as a preliminary assessment of the case study buildings. The pushover curves of the case study buildings are presented in [Figure 9](#), in terms of the base shear against the roof drift ratio. [Figure 9](#) also shows the behaviour of the critical storey, *i.e.* where soft-storey mechanism occurred, of each of the case study buildings. It is clearly shown by the pushover curves that the presence of masonry infills is able to cause more complex inelastic behaviour of the steel buildings, hence leads to increased difficulty in the establishment of the FNN models and estimating accurately the structural response.

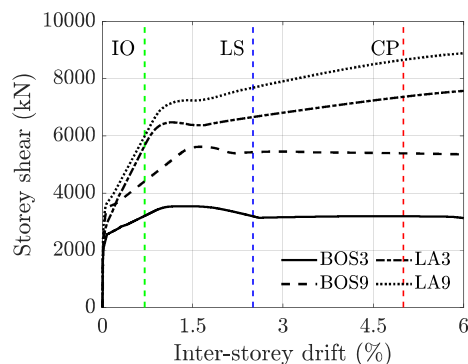


Figure 9. Pushover curves of the case study buildings at the storey level.

5.3 Definition of Limit States and IDR Criteria

Three limit states were adopted in this case study, which were defined based on the MIDR of steel moment-resisting frames recommended by FEMA 365 [29]. The criteria are presented in [Table 6](#).

Table 6. The IDR criteria adopted in this study.

Limit state	IO	LS	CP
IDR TH (%)	0.7	2.5	5.0

The IDR THs were 0.7, 2.5 and 5%, respectively for the Immediate Occupancy (IO), Life Safety (LS) and Collapse Prevention (CP) limit state. The IDR criteria are also demonstrated in [Figure 9](#) in order to investigate the behaviour of the case study buildings at each limit state at the storey level. It was found that all case study buildings reached the IO limit state prior to the peak point corresponding to the onset of failure of masonry infills, while at the LS and CP limit state, the steel buildings all have passed the peak strength point and experienced strength degradation due to failure of masonry infills.

5.4 Selection of Ground Motions and Intensity Measures

As mentioned in Section 3, the GM database in FEMA P695 [27] were adopted to generate the training data, which were obtained from the PEER database [28]. It should be mentioned that the GM database originally contained 28 near-fault GMs and 22 far-field GMs, however, one of the far-field GMs was missing from the PEER database and was excluded from the present study, leading to a database of 49 GM records. Besides, only the first horizontal component of each ground motion was considered in this study for the development of fragility curves for the demonstration of the proposed [method_{\[DSL7\]}](#).

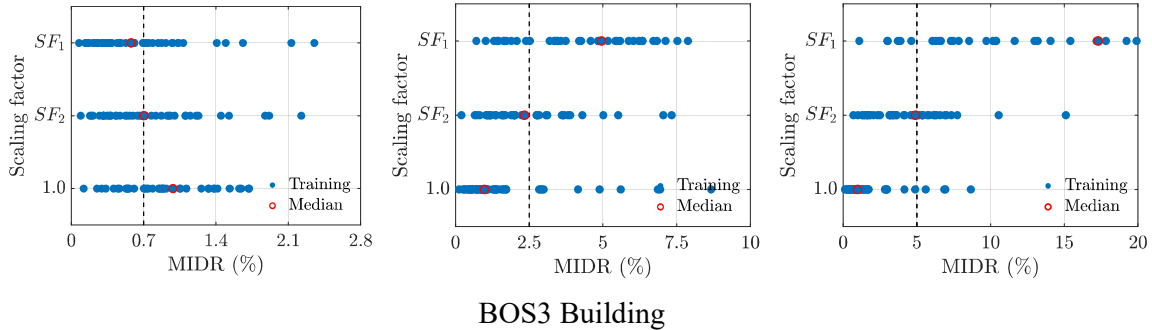
5.5 Preparation of Training Data

The procedure of generating training and validation datasets proposed in Section 3.2 were repeated for each steel building at each limit state. The median MIDRs and scaling factors calculated to scale the GM records were summarised in [Table 7](#).

Table 7. Median MIDRs and scaling factors adopted to generate the training data.

		BOS3	BOS9	LA3	LA9
Unscaled	$MIDR_{med,1}$ (%)	0.983	0.720	0.483	0.567
IO limit state	$MIDR_{med,2}$ (%)	0.578	0.707	0.912	0.742
	SF_1	0.712	0.973	1.449	1.234
	SF_2	0.805	0.956	1.242	1.179
LS limit state	$MIDR_{med,2}$ (%)	4.952	4.100	5.686	3.790
	SF_1	2.542	3.474	5.175	4.408
	SF_2	1.714	2.438	2.992	3.185
CP limit state	$MIDR_{med,2}$ (%)	17.288	9.706	12.861	8.838
	SF_1	5.085	6.948	10.350	8.816
	SF_2	2.516	4.239	5.281	5.613

[Figure 10](#) shows the data generated for training the FNN models based on the scaling factors in [Table 7](#). As can be seen, the definition of SF_1 effectively led to a group of MIDR data that in combination with the unscaled MIDRs forming a balanced training dataset, due to the significant nonlinearity of the structural response. It should be mentioned that in this case, ‘balanced data’ does not require equally divided MIDR data, but the numbers of data leading to ‘Safe’ and ‘Unsafe’ cases are not supposed to considerably differ from each other.



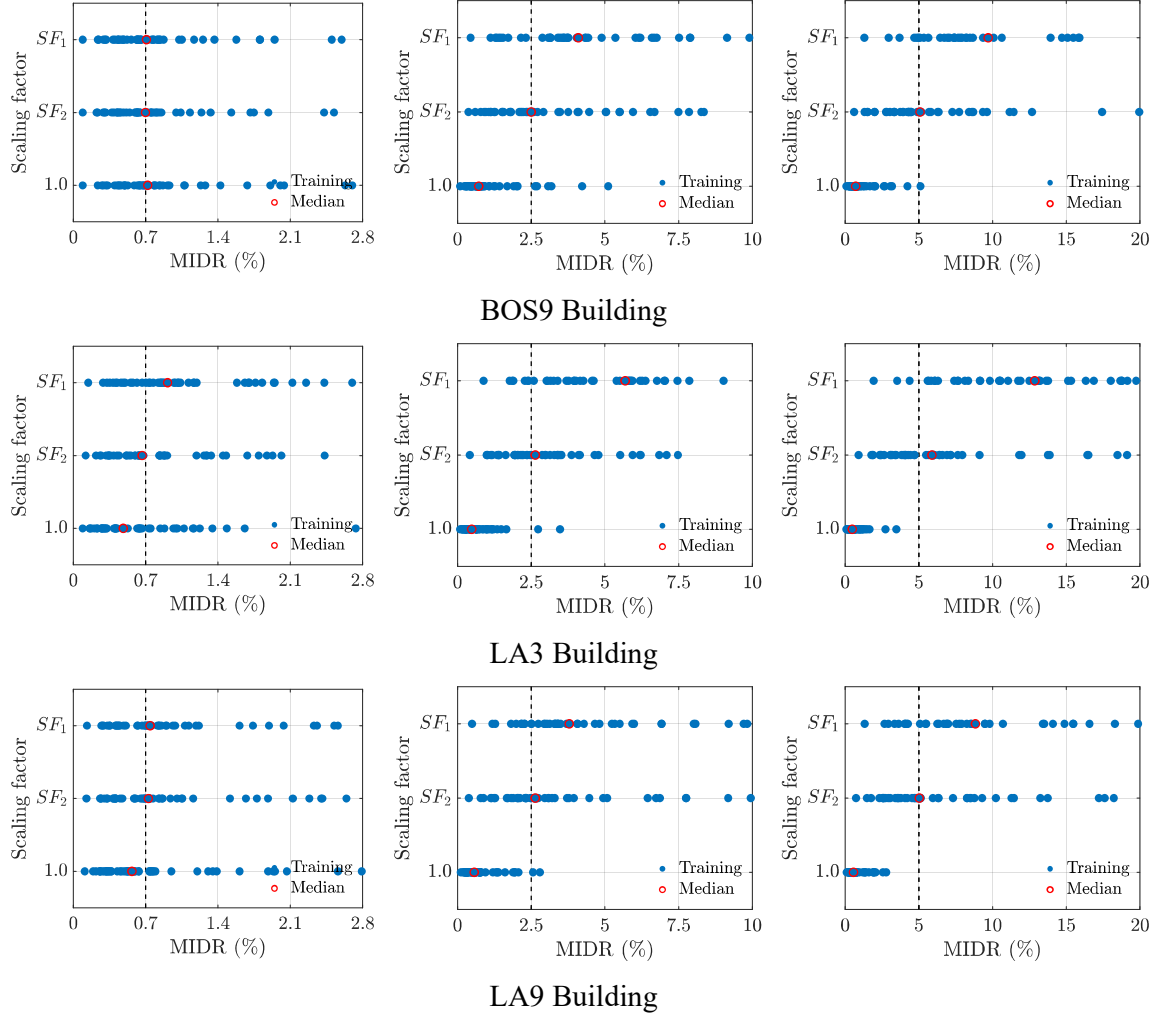
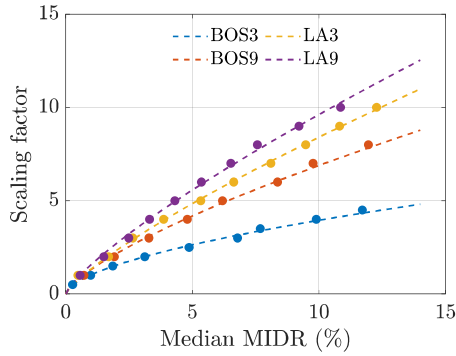


Figure 10. Distribution of the training data generated for each case study steel frame with respect to the target IDR limit (indicated as the black dash line).

The use of an exponential expression for the definition of SF_2 is explained in Figure 11, which shows clearly that the relationship between the median MIDR based on the selected GM database and the scaling factor can be well approximated by an exponential curve for all the steel frames in this study. Additionally, it is also shown in Figure 10 that the adopted SF_2 effectively led to median values of MIDR approximately equal to the target IDRs, suggesting that the validation data were also balanced.

Furthermore, as shown in the case of BOS9 and LA9 buildings at the IO limit state in Figure 10, the median of the obtained MIDRs under unscaled GM records ($MIDR_{med,1}$) can be close to the target IDR (IDR_{LS}), in which cases the scaling factors SF_1 and SF_2 are likely to be

equal to one. As a consequence, the patterns of the data obtained with the scaling factor 1.0 (unscaled), SF_1 and SF_2 can be similar to each other, which may lead to repeated training data and compromised accuracy of the trained FNN models. However, as this circumstance is not frequent and can be easily addressed by applying a suitable scaling factor instead of 1.0 to generate the first dataset, it is considered not affecting significantly the capability of the proposed framework.



$$\text{BOS3: } y = 1.028x^{0.585} (R^2 = 0.995)$$

$$\text{BOS9: } y = 1.313x^{0.720} (R^2 = 0.997)$$

$$\text{LA3: } y = 1.346x^{0.800} (R^2 = 0.999)$$

$$\text{LA9: } y = 1.570x^{0.787} (R^2 = 0.997)$$

Figure 11. Exponential relationship between the scaling factor and the median MIDR.

5.6 Training of the FNN Models

Prior to the training of the FNN models, a few times of trial training were conducted and it was found that a hidden layer with ten nodes was sufficient in this study to allow adequate accuracy of the FNN models for all case study buildings. The ratio between training and validation data was decided to be 70/30 to avoid over-fitting, and for each training dataset the selection of validation data remained unchanged during the exploration of all potential fragility curves. The training process was conducted for a sufficient number of times for each steel building at each limit state, such that all potential fragility curves were obtained. When training the FNN models, their performance in estimating correctly each class was evaluated against the validation data and only those achieved at least 90% accuracy in estimating both the ‘Safe’ and ‘Unsafe’ cases were adopted for deriving fragility curves, otherwise the FNN models were abandoned.

6 Derivation and Comparisons of Fragility Curves

In this section, comparisons were made between the fragility curves obtained through conventional incremental dynamic analysis (IDA) and the proposed method using MSA. For both cases, the MIDR was adopted as the EDP. Besides, three commonly adopted IMs were used here, including PGA, $S_a(T_1)$ and CAV, in order to illustrate the flexibility in the choice of IMs when using the proposed framework to derive fragility curves.

6.1 Incremental Dynamic Analysis

The IDA performed in this study considered the same GM records used to generate training data in the previous section and a small incremental step of 0.1 for the scaling factor (*i.e.* the scaling factor of 0.1, 0.2, ... were used until the exceedance of the target limit state). Therefore, the adopted IDA was sophisticated and time-consuming, but was supposed to result in high accuracy of the fragility curves. The fragility curves obtained based on the IDA method are presented in [Figure 13 to 16](#).

6.2 The Proposed FNN-Based Method

The fragility curves obtained using the proposed method based on MSA were also presented in [Figure 13 to 16](#). By comparing the fragility curves obtained by the two methods, it can be seen that in the majority of cases, the results obtained from the proposed method provided a good approximation of the fragility curves obtained from the IDA. This suggested that the proposed method was able to produce similar results to the sophisticated IDA adopted in this study, but at a significantly reduced computational cost. Besides, the accuracy of the proposed method did not vary significantly among the adopted IMs, highlighting its flexibility in the selection of IMs for the derivation of fragility curves.

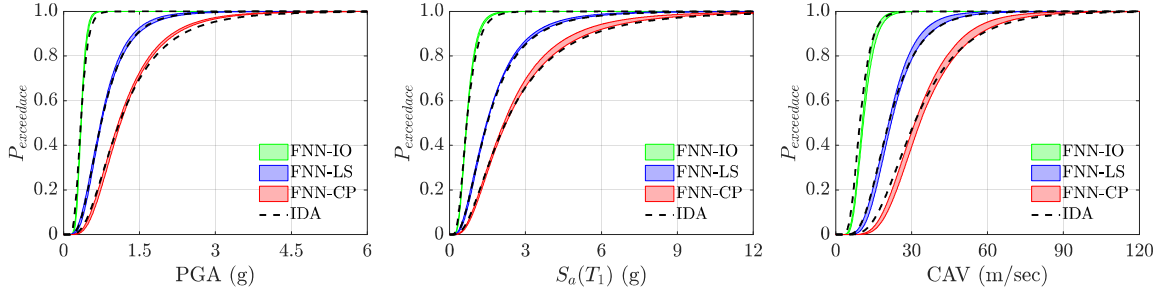


Figure 13. Comparisons of fragility curves for the BOS3 building.

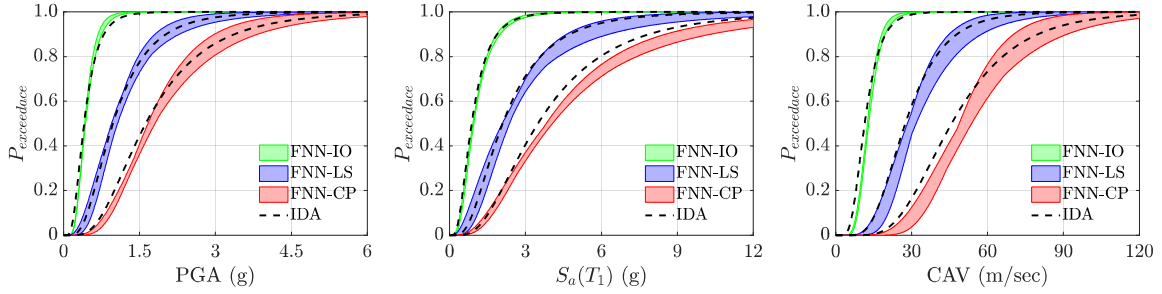


Figure 14. Comparisons of fragility curves for BOS9 building.

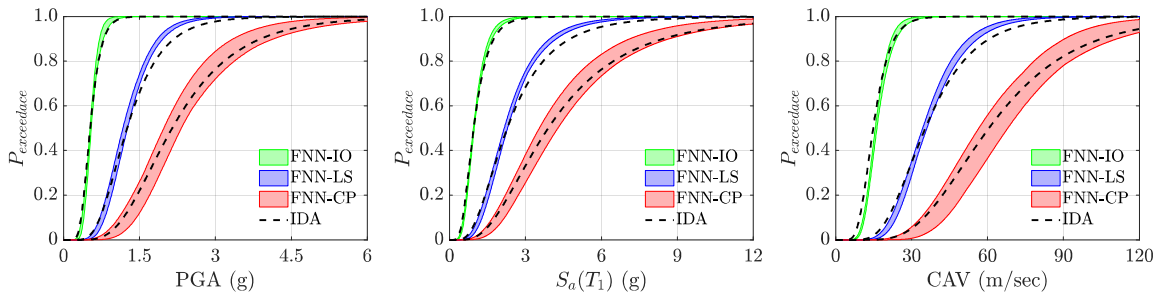


Figure 15. Comparisons of fragility curves for LA3 building.

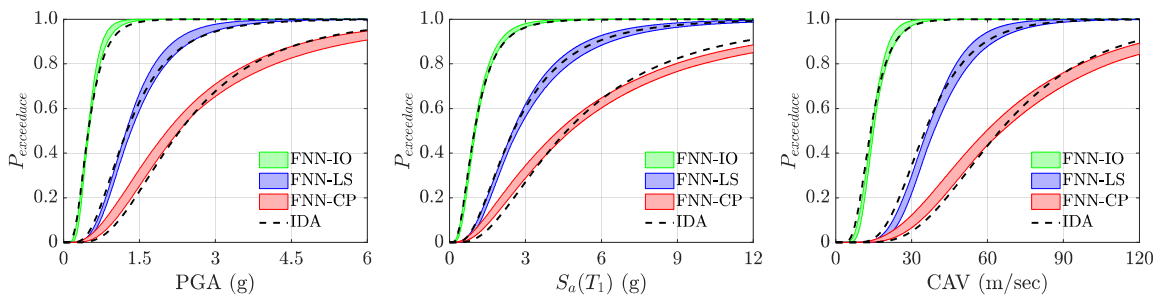


Figure 16. Comparisons of fragility curves for LA9 building.

Additionally, to compare the computational cost demanded by the IDA and the proposed method, the number of total NTHAs required was summarised in [Table 8](#). In the table, ‘standalone’ indicates the number of NTHA required to derive each of the corresponding

fragility curve independently, while ‘cumulative’ indicates the cumulative number of NTHA required when deriving the state-dependent fragility curves simultaneously. As shown in [Table 8](#), the proposed method required significantly smaller numbers of NTHA compared to the IDA adopted in this study, particularly when the fragility curves corresponding to all limit states were of interest. The time required to run the FNN models during the MSA was found to be negligible compared to the time for the NTHA, hence was not considered in [Table 8](#).

Table 8. Summary of number of NTHA required to derive each fragility curves using the IDA and the proposed method.

Building	Limit state	No. of NTHA required			
		IDA		Proposed	
		Standalone	Cumulative	Standalone	Cumulative
BOS3	IO	447	447	147	147
	LS	1005	1005	147	245
	CP	1518	1518	147	343
BOS9	IO	561	561	147	147
	LS	1314	1314	147	245
	CP	2159	2159	147	343
LA3	IO	673	673	147	147
	LS	1645	1645	147	245
	CP	2796	2796	147	343
LA9	IO	667	667	147	147
	LS	1668	1668	147	245
	CP	3036	3036	147	343

7 Conclusions

This paper presented a machine learning-based method to derive the fragility curves of existing steel frames, considering also the influence of masonry infills. The proposed method utilised FNN to estimate the failure states of structures for the limit states under consideration, aiming at reducing considerably the computational cost as in the conventional IDA. Four steel moment frames were adopted as the case study buildings to demonstrate the proposed method, which were considered representatives of low- and mid-rise existing steel moment

frames designed for low and high seismicity. Comparisons were made between the fragility curves obtained from conventional IDA using 49 GMs at small incremental steps, which was time-consuming but led to high accuracy of fragility curves, and the fragility curves obtained using the proposed method.

The comparisons showed that the proposed method led to results that are very close to the fragility curves obtained from the sophisticated IDA performed in this study. The differences were considered acceptable, especially when considering the influence of masonry infills on the overall structural response. Besides, the flexibility of the proposed method in terms of the choice of IMs was also illustrated, where for the IMs considered in this study (PGA , $S_a(T_1)$ and CAV), the proposed method exhibited approximately the same performance in the derivation of fragility curves. More importantly, the suggested approach requested much less computational demand compared to the conventional IDA, as the number of required NTHA for generating training data was significantly smaller compared to the case of IDA. Therefore, utilizing efficiently the capabilities of machine learning techniques, the proposed method can be adopted as an effective replacement of the conventional IDA in the fragility analysis of existing steel frames, particularly when the effects of masonry infills are taken into account.

Reference

1. Porter K, Kennedy R, Bachman R. Creating fragility functions for performance-based earthquake engineering. *Earthquake Spectra*. 2007;23(2): 471-489. <https://doi.org/10.1193/1.2720892>
2. Vamvatsikos D, Cornell CA. Incremental dynamic analysis. *Earthquake Engineering and Structural Dynamics*. 2002;31(3): 491-514. <https://doi.org/10.1002/eqe.141>
3. Baker JW. Efficient analytical fragility function fitting using dynamic structural analysis. *Earthquake Spectra*. 2015;31(1): 579-599. <https://doi.org/10.1193/021113EQS025M>

4. Sun H, Burton HV, Huang H. Machine learning applications for building structural design and performance assessment: State-of-the-art review. *Journal of Building Engineering*. 2021;33: 101816. <https://doi.org/10.1016/j.jobbe.2020.101816>
5. Murphy KP. *Machine learning: a probabilistic perspective*. Massachusetts: MIT press; 2012.
6. Xie Y, Ebad Sichani M, Padgett JE, DesRoches R. The promise of implementing machine learning in earthquake engineering: A state-of-the-art review. *Earthquake Spectra*. 2020;36(4): 1769-1801. <https://doi.org/10.1177/8755293020919419>
7. Falcone R, Lima C, Martinelli E. Soft computing techniques in structural and earthquake engineering: a literature review. *Engineering Structures*. 2020;207:110269. <https://doi.org/10.1016/j.engstruct.2020.110269>
8. Mitropoulou CC, Papadrakakis M. Developing fragility curves based on neural network IDA predictions. *Engineering Structures*. 2011;33(12): 3409-3421. <https://doi.org/10.1016/j.engstruct.2011.07.005>
9. Seo J, Dueñas-Osorio L, Craig JI, Goodno BJ. Metamodel-based regional vulnerability estimate of irregular steel moment-frame structures subjected to earthquake events. *Engineering Structures*. 2012;45: 585-597. <https://doi.org/10.1016/j.engstruct.2012.07.003>
10. Morfidis K, Kostinakis K. Seismic parameters' combinations for the optimum prediction of the damage state of R/C buildings using neural networks. *Advances in Engineering Software*. 2017;106: 1-6. <https://doi.org/10.1016/j.advengsoft.2017.01.001>
11. Moradi S, Burton HV. Response surface analysis and optimization of controlled rocking steel braced frames. *Bulletin of Earthquake Engineering*. 2018;16(10): 4861-4892. <https://doi.org/10.1007/s10518-018-0373-1>

12. Khojastehfar E, Beheshti-Aval SB, Zolfaghari MR, Nasrollahzade K. Collapse fragility curve development using Monte Carlo simulation and artificial neural network. *Proceedings of the Institution of Mechanical Engineers, Part O: Journal of Risk and Reliability*. 2014;228(3): 301-312. <https://doi.org/10.1177/1748006X13518524>
13. Jough FK, Şensoy S. Prediction of seismic collapse risk of steel moment frame mid-rise structures by meta-heuristic algorithms. *Earthquake Engineering and Engineering Vibration*. 2016;15(4): 743-757. <https://doi.org/10.1007/s11803-016-0362-9>
14. Burton HV, Sreekumar S, Sharma M, Sun H. Estimating aftershock collapse vulnerability using mainshock intensity, structural response and physical damage indicators. *Structural Safety*. 2017;68: 85-96. <https://doi.org/10.1016/j.strusafe.2017.05.009>
15. Zhang Y, Burton HV, Sun H, Shokrabadi M. A machine learning framework for assessing post-earthquake structural safety. *Structural safety*. 2018;72: 1-6. <https://doi.org/10.1016/j.strusafe.2017.12.001>
16. Kiani J, Camp C, Pezeshk S. On the application of machine learning techniques to derive seismic fragility curves. *Computers & Structures*. 2019;218: 108-122. <https://doi.org/10.1016/j.compstruc.2019.03.004>
17. Noh NM, Liberatore L, Mollaioli F, Tesfamariam S. Modelling of masonry infilled RC frames subjected to cyclic loads: State of the art review and modelling with OpenSees. *Engineering Structures*. 2017;150: 599-621. <https://doi.org/10.1016/j.engstruct.2017.07.002>
18. Di Sarno L, Wu JR. Seismic assessment of existing steel frames with masonry infills. *Journal of Constructional Steel Research*. 2020;169: 106040. <https://doi.org/10.1016/j.jcsr.2020.106040>
19. Di Sarno L, Freddi F, D'Aniello M, Kwon OS, Wu J-R, Gutiérrez-Urzúa F, Landolfo R, Park J, Palios X, Strepelias E. Assessment of existing steel frames: Numerical study,

- pseudo-dynamic testing and influence of masonry infills. *Journal of Constructional Steel Research*. 2021;185: 106873. <https://doi.org/10.1016/j.jcsr.2021.106873>
20. Nocedal J, Wright SJ. *Numerical Optimization*. New York: Springer; 2006.
21. Gupta A, Krawinkler H. Behavior of ductile SMRFs at various seismic hazard levels. *Journal of Structural Engineering*. 2000;126(1): 98-107. [https://doi.org/10.1061/\(ASCE\)0733-9445\(2000\)126:1\(98\)](https://doi.org/10.1061/(ASCE)0733-9445(2000)126:1(98))
22. Gutierrez-Urzua F, Freddi F, Di Sarno L. Comparative analysis of code-based approaches for seismic assessment of existing steel moment resisting frames. *Journal of Constructional Steel Research*. 2021;181:106589. <https://doi.org/10.1016/j.jcsr.2021.106589>
23. McKenna F, Fenves GL, Scott MH. *Open System for Earthquake Engineering Simulation*. University of California, Berkeley, 2000.
24. Liberatore L, Decanini LD. Effect of infills on the seismic response of high-rise RC buildings designed as bare according to Eurocode 8. *Ingegneria sismica*. 2011;3: 7-23.
25. Di Sarno L, Freddi F, D'Aniello M, Kwon OS, Wu J-R, Gutiérrez-Urzúa F, Landolfo R, Park J, Palios X, Strepelias E. Assessment of existing steel frames: Numerical study, pseudo-dynamic testing and influence of masonry infills. *Journal of Constructional Steel Research*. 2021;185: 106873. <https://doi.org/10.1016/j.jcsr.2021.106873>
26. Thaler D, Stoffel M, Markert B, Bamer F. Machine-learning-enhanced tail end prediction of structural response statistics in earthquake engineering. *Earthquake Engineering and Structural Dynamics*. 2021;50(8): 2098-2114. <https://doi.org/10.1002/eqe.3432>
27. Federal Emergency Management Agency. FEMA P695. *Quantification of Building Seismic Performance*. Applied Technology Council: Redwood City, California; 2009.
28. Pacific Earthquake Engineering Research Center. *PEER NGA-West2 Database*. University of California, Berkeley, 2013.

29. Federal Emergency Management Agency. FEMA 365. *Prestandard and Commentary for the Seismic Rehabilitation of Buildings*. American Society of Civil Engineers: Reston, Virginia; 2000.